Spatially Templated Nanolines of Ru and RuO2 by Sequential Infiltration Synthesis

Reference:

Nithin Poonkottil, Eduardo Solano, Arbresha Muriqi, Matthias M. Minjauw, Matthias Filez, Michael Nolan, Christophe Detavernier, and Jolien Dendooven*; Chem. Mater. 2022, XXXX, XXX, XXX-XXX

Full text (Publisher's DOI): doi.org/10.1021/acs.chemmater.2c01866

Spatially Templated Nanolines of Ru and RuO_2 by Sequential Infiltration Synthesis

Nithin Poonkottil, † Eduardo Solano,$ Arbresha Muriqi, ‡ Matthias M. Minjauw, † Matthias Filez, †Michael Nolan, ‡ Christophe Detavernier† and Jolien Dendooven†,*

† Department of Solid State Sciences, COCOON, Ghent University, Krijgslaan 281/S1, B-9000 Ghent, Belgium

$ NCD-SWEET beamline, ALBA Synchrotron Light Source, Cerdanyola del Vallès 08290, Spain

‡ Tyndall National Institute, University College Cork, Lee Maltings, T12 R5CP Cork, Ireland

* Corresponding author: jolien.dendooven@ugent.be

Abstract

Nanoscale patterning of inorganics is crucial for the fabrication of advanced electronic, photonic and energy devices. The emerging sequential infiltration synthesis (SIS) method fabricates nanofeatures by block-selective vapor-phase growth in block copolymer templates with tunable patterns. Yet, SIS has been demonstrated mainly for Al_2O_3 and few other metal oxides, while deriving metal nanostructures from a single SIS process is a challenge. Here, we present SIS of Ru metal in polystyrene-block-polymethylmethacrylate (PS-b-PMMA) templates without any pre-treatment, using alternating infiltration of RuO_4 and H_2. RuO_4 interacts selectively and strongly with the aromatic C=C and C-H groups in PS, leaving PMMA domains inert. Density functional theory calculations corroborate that PS-RuO_4 interaction is energetically favorable, with a calculated interaction energy of -1.65 eV, whereas for PMMA-RuO_4 the calculated energy of -0.05 indicates an unfavorable interaction. Morphological analysis on the di-BCP after the RuO_4-H_2 process indicates increase in contrast as a function of SIS cycles and templated Ru incorporation. The crystalline nature of the Ru deposits is confirmed using grazing incidence wide angle X-ray scattering. Plasma aided removal of the organic components yields Ru nanolines with lateral dimensions of ca. 20 nm. We further highlight the broad potential of RuO_4 as reactant for SIS by generating RuO_2 nanopatterns via alternating RuO_4 and methanol infiltration.

1. Introduction

Ruthenium (Ru) is a candidate to replace copper in future interconnects. Its properties, including low bulk resistivity (ca. 7μΩcm), very high work function (> 4.7 eV), good chemical, and thermal stability, oxygen diffusion barrier property, etc. have driven significant research towards the synthesis of Ru by various techniques. In addition, Ru has very good adhesion with copper and is considered as a replacement for TiN capacitor electrodes in dynamic random access memories (DRAM). Thin ruthenium films also find applications in separating the magnetic layers in antiferromagnetically coupled (AFC) magnetic recording media as well as in magnetic random access memories (MRAMs).[1-4] The applications of Ru in catalysis are also well established.[5-6]

Complementarily, ruthenium dioxide (RuO_2), the most stable oxide of Ru, also has an extremely low resistivity value (35 μΩ.cm), is chemically stable, and has a work function that is even greater than metallic Ru (5.1 eV for RuO_2 and 4.1 eV for Ru).[7-8] RuO_2 is a useful heterogenous catalyst for low temperature dehydrogenation of molecules like HCl, NH_3, methanol etc. Over the past 4 decades, RuO_2 has been used as a dimensionally stable anode (DSA) for the chlorine-alkali electrocatalysis.[9-10]Atomic layer deposition (ALD) is a very efficient route towards the synthesis of conformal and precise coatings on to high aspect ratio structures.[11-16] For this reason, there have been many reports on deposition of Ru[1, 17-18] and RuO_2 [17, 19-20] by ALD.

Vapor phase infiltration (VPI) or sequential infiltration synthesis (SIS) is a versatile technique in which an organic layer (typically polymer-based) is sequentially infiltrated with the ALD precursors and reactants. The diffusion of the precursors into the polymer followed by the subsequent reaction leads to the formation of an inorganic material within the polymer film. This modifies the original physicochemical properties of the starting polymer. Self-assembled block copolymers (BCP) provide a unique feature for an SIS process: the selective binding of ALD precursors to one of the BCP's domains can be used to build inorganic nanostructures or hard mask layers, which can be generally used in lithographic applications.[21-25] For such applications, the difference in selectivity of the ALD precursors between the domains of the BCP is crucial, ensuring that only one of the blocks is infiltrated while the other maintains its original properties. The creation of inorganic nanostructures inside the reactive block can be triggered by a cyclic introduction of the precursors and suitable co-reactants. To saturate the polymer free volume with the inorganic substance of interest, one can experiment with injection times (precursor and/or co-reactant) or the number of SIS cycles. The polymer matrix can be burned away after infiltration with a simple plasma treatment or calcination leaving the patterned inorganic material thanks to the original BCP morphology.[22]

Although SIS reactions borrow ALD precursors and are usually performed in ALD reactors, the processing parameters can differ hugely compared to ALD. Contrary to ALD, the exposure times are usually much longer in SIS to promote efficient diffusion of precursor molecules through the pore volume of the starting polymer. The other major requirements of a SIS process involve low substrate temperature to avoid polymer degrading, the ability of the precursors to diffuse easily and react with the polymer domain of interest.[26] Note that solubility and diffusivity are two important parameters that govern the faith of a SIS process. Metal precursors should be capable of dissolving into the polymer free volume and possess a reasonable diffusivity. Similarly, solubility is a very important factor for successful SIS experiments. Unless the precursor molecules are soluble in the polymer film, the retention of precursor molecules in the polymer films will be difficult and chances are that the precursor molecules out-diffuse during the pump/purge step.[26-27] Nevertheless, interesting applications of infiltration of inorganic materials into polymers are seen in the literature including, increased toughness of spider silk[28], improved mechanical properties of collagen[29], contrast enhancement of block co-polymers[30-32], solvent separation membranes[33], conductivity improvement[34-35] and so on.[27, 36] SIS in general has been applied to lithography[23-24, 37-38], protein separations[39], optical coatings[40], oil sorption[41] etc. The other potential applications and features of SIS or infiltration in general, have been review already.[42-44]

The currently available library of SIS chemistry is quite limited with reports arising from mainly metal oxides, with Al_2O_3 SIS using trimethyl aluminium (TMA) and H_2O being the most explored.[25, 45] Recent reports demonstrate the infiltration of Al_2O_3 nanostructures using O_3[22] and O_2 plasma[46] as co-reactants in combination with TMA. Oxides such as SiO_2[24], ZnO[24, 47], SnO_2[37], TiO_2[48], In_2O_3[45], Ga_2O_3[45] are also explored in the field of SIS. However, there is only one report on direct metal SIS up until now, where the SIS of tungsten metal is demonstrated, but with Al_2O_3 acting as a seed layer.[24] Prior to tungsten SIS cycles, a few Al_2O_3 SIS cycles are usually done, resulting in alumina filling of the polymer free volume. For applications that require pure metal with no extraneous contaminants, this method can be troublesome. This clearly demonstrates the difficulty in the area of metal SIS, which could be due to the high deposition temperatures required, the necessity of plasma or ozone as co-reactants for most of metal depositions, which can degrade the polymer, or the bulky precursors that may not be able to freely diffuse into the polymer volume. Another crucial requirement is to have a distinct selectivity difference between the polymers employed, presenting another challenge.

In this context, we demonstrate the first SIS process for ruthenium metal at low infiltration temperature of 120 °C in a block co-polymer, without requiring any pre-treatment. This SIS process for Ru was derived from an ALD process developed by our research group, using an inorganic RuO_4 as Ru source and H_2 as co-reactant.[49] Previously, RuO_4 exposures in liquid

phase have been used to (selectively) stain (block co) polymers especially for increasing their contrast in electron microscopy.[50-52] Herein, we translate this knowledge from liquid phase to vapor phase via infiltration reactions using the RuO_4-H_2 process studied on polystyrene homopolymer (PS) and PMMA homopolymer (PMMA) showing that RuO_4 selectively reacts with PS, but not with PMMA. This opens up opportunities for creating Ru nanopatterns using a polystyrene-block-polymethylmethacrylate (PS-b-PMMA) template, where Ru is exclusively deposited inside the PS domain to form a hybrid material. Finally, the polymer template can be removed to obtain Ru nanostructures, mimicking the original PS domain. To the best of our knowledge, this is the first report of metal SIS without any pre-treatment. We further show that, similar to Ru SIS, RuO_2 SIS can be achieved utilizing the methanol-RuO_4 ALD process, wherein also the PS domains act as the reactive block and PMMA stays inert. In prior SIS reports with PS-b-PMMA, the ALD precursors (metal organic and organometallic) were shown to react with PMMA explained by the interaction with the C=O group present, but the PS component remains unaffected due to the absence of any functional groups[23]. The Ru and RuO_2 processes presented here, on the other hand, occur only in the PS domain. The experimental observations on the selectivity difference between PS and PMMA are corroborated by first principles density functional theory (DFT) studies. Different aspects of the infiltration process such as selectivity, crystallinity of the infiltrated Ru, and morphology are extensively studied, and a plausible reaction mechanism is proposed.

2. Results and discussion

In the current work, three different polymers are used, polystyrene (PS, Figure 1a) and polymethyl methacrylate (PMMA, Figure 1b) homopolymers and polystyrene-block-polymethyl methacrylate (PS-b-PMMA, Figure 1c) di-block copolymer thin films, all of which are prepared by spin coating. The different synthetic approaches for block copolymers have been reviewed elsewhere.[53] In this work, self-assembled PS-b-PMMA films with a lamellar morphology were used.

An overview of the developed SIS process for Ru is depicted in Figure 1d-g. The starting substrate represents a self-assembled di-block copolymer (PS-b-PMMA in our case) consisting of both PS and PMMA components. The block copolymer is first exposed to RuO_4 (an inorganic Ru source) molecules inside an ALD reactor. This allows the infiltration/diffusion of RuO_4 molecules selectively into the PS component of the block copolymer, at the same time leaving the PMMA unreacted. The interaction of PS with RuO_4 chemically modifies the PS component and an extra H_2 pulse is followed after the pumping of unreacted RuO_4 molecules. This is followed by the introduction H_2 gas that reduces the infiltrated RuO_4 (RuO_x) molecules to metallic Ru. This RuO_4-H_2 SIS cycle is thus repeated until the required amount of Ru loading inside the polymer free volume is achieved. Now, an inorganic-organic hybrid

layer is present, which comprises Ru as the inorganic component and PS as the organic component, in addition to the unmodified PMMA. Finally, the organic components of the polymer film are removed by a plasma treatment (H_2 plasma in our case) which leads to the formation of Ru nanostructures (Figure 1g) that resemble the reactive block (PS) of the starting PS-b-PMMA block copolymer template.

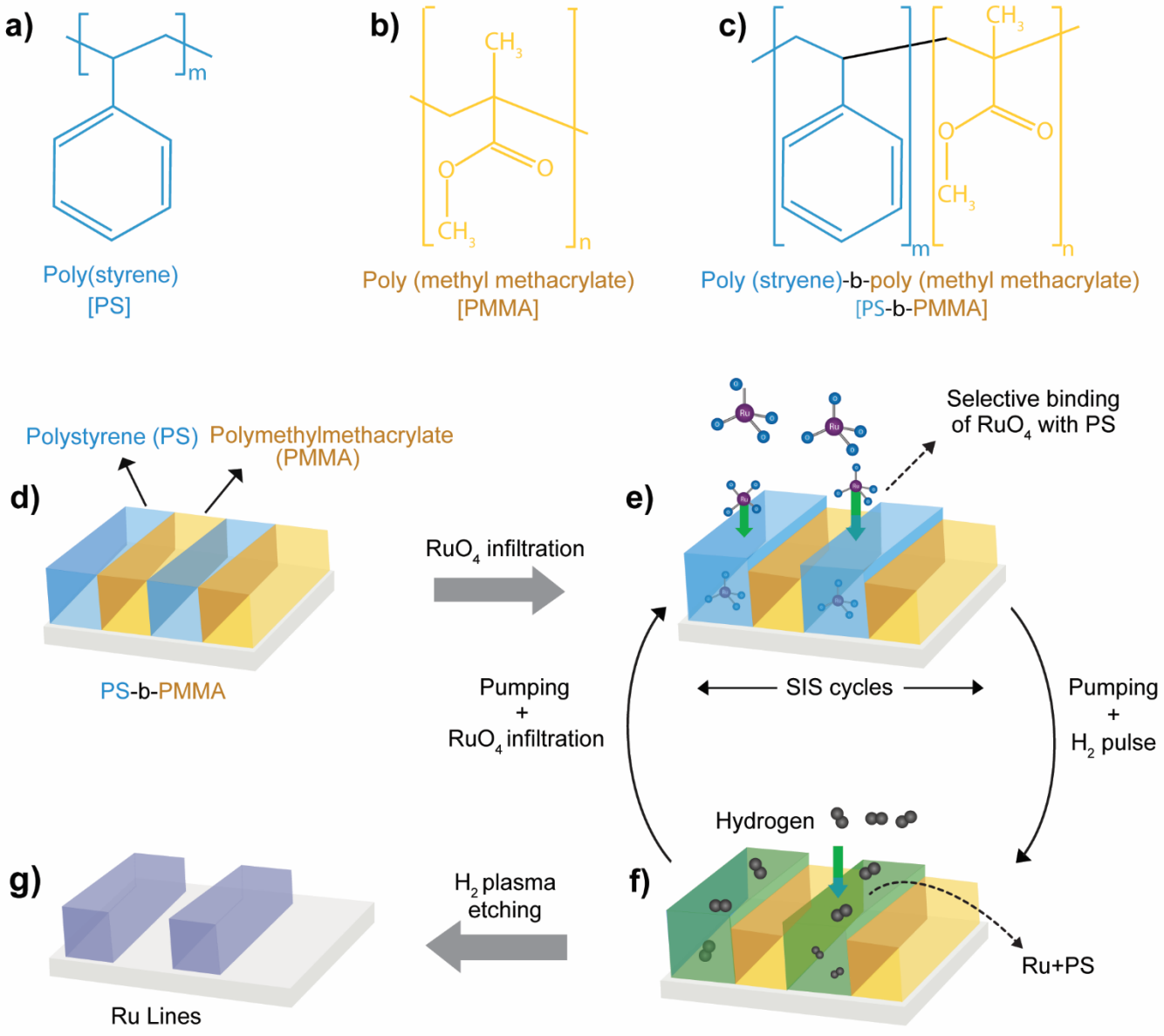

Figure 1: Chemical structures of the different polymers used in this study. **a)** Polystyrene (PS) homopolymer, **b)** Polymethyl methacrylate (PMMA)homopolymer and **c)** Polystyrene-block- polymethyl methacrylate (PS-b-PMMA) di-block copolymer. Simplified illustration of the Ru SIS process. **d)** Starting PS-b-PMMA template containing both PS and PMMA domains. **e)** Selective RuO_4 infiltration into PS domains, this interaction causes swelling of these

domains, as will be discussed later (note the height increase of the domains compared to bare di-BCP). **f)** chemical modification of the PS domain followed by H_2 pulse to form metallic Ru inside PS domains. **g)** An H_2 plasma etch step to remove the BCP template to generate Ru nanopatterns on the substrate surface.

2.1. Selective infiltration into PS domains

In order to achieve Ru SIS, we rely on the previously developed Ru ALD process from our group, using RuO_4 as the Ru precursor, and H_2 gas as the co-reactant.[49] This process allows deposition of Ru at substrate temperatures ranging from 100°C to120°C, which is ideal to work with polymers such as PS and PMMA. For the Ru SIS, we chose 120°C as the working substrate temperature as this temperature is above the glass transition temperature both the PS (100°C) and PMMA (105°C) homopolymers, and this ensures maximum free volume of these polymers. In order to validate the difference in interaction of RuO_4 with PS and PMMA, first PS and PMMA homopolymer films were spin coated and transferred to the ALD chamber. Prior to SIS, the polymer samples were kept inside the ALD reactor under vacuum for an hour at a temperature of around 100°C to remove any residual solvents or gases. Then these polymers were exposed to RuO_4 at a pressure of ca. 2 mbar and H_2 gas at a pressure of ca. 5 mbar in a cyclic manner. Higher pressures compared to conventional ALD are achieved by the static mode of exposures, as this would allow for significant diffusion of the reacting molecules into the bulk of the polymers.

The infiltration process was monitored *in situ* using spectroscopic ellipsometry (SE) to observe the changes in the psi (Ψ) value as this can be used as an identification of the selectivity.[54] As shown in Figure 2a, on PS the Ψ value changes from the very first cycle, but on the other hand it remains unchanged on PMMA films even after 200 cycles. This in turn indicates the selective reaction of the RuO_4 precursor with PS compared to PMMA, opening up opportunities for selective infiltration of the PS component in PS-b-PMMA di-block copolymer, satisfying the necessary conditions for BCP based lithography, as stated before. The selectivity was corroborated using XPS, after 30 SIS cycles (highest number of SIS cycles used in this work as higher cycles might lead to ALD like growth on the surface rather than infiltration like process). The Ru 3d XPS region is presented in Figure 2b. Due to the overlap of Ru $3d_{3/2}$ with C 1s, extracting quantitative information was troublesome. However, it can be immediately seen that on PMMA, there was no Ru $3d_{5/2}$ peak present, but on the other hand on PS and PS-b-PMMA it was present.

The selective infiltration of RuO_4 with PS was again revealed by the Ru 3p peaks (where there is no overlap with C1s) in **Figure 2c**. PS and PS-b-PMMA gave rise to Ru 3p peaks after the SIS process, whereas no Ru 3p peak could be observed on PMMA. Complementary XRF

(**Figure S1)** measurements also indicated a clear Ru signal on the PS and PS-b-PMMA films but not on the PMMA films. To confirm the presence of Ru in the free volume (bulk) of the polymers, XPS depth profiling (**Figure 2d**) was performed. The irregular pattern of C1s signal in PMMA is originating from the higher noise level in the C1s data of the PMMA sample. The higher noise makes it difficult to realize the same background for the C1s peak at different sputter levels. Nevertheless, the Ru 3p intensity on both PS and PS-b-PMMA tends to follow the same trend as C 1s peak in these polymers, which indicates the binding of Ru with the carbon in the polymer and clear indication of Ru present in the bulk of the polymer, in agreement with the in situ ellipsometry data. In short, excellent selective infiltration of RuO_4 molecules into PS could be achieved.

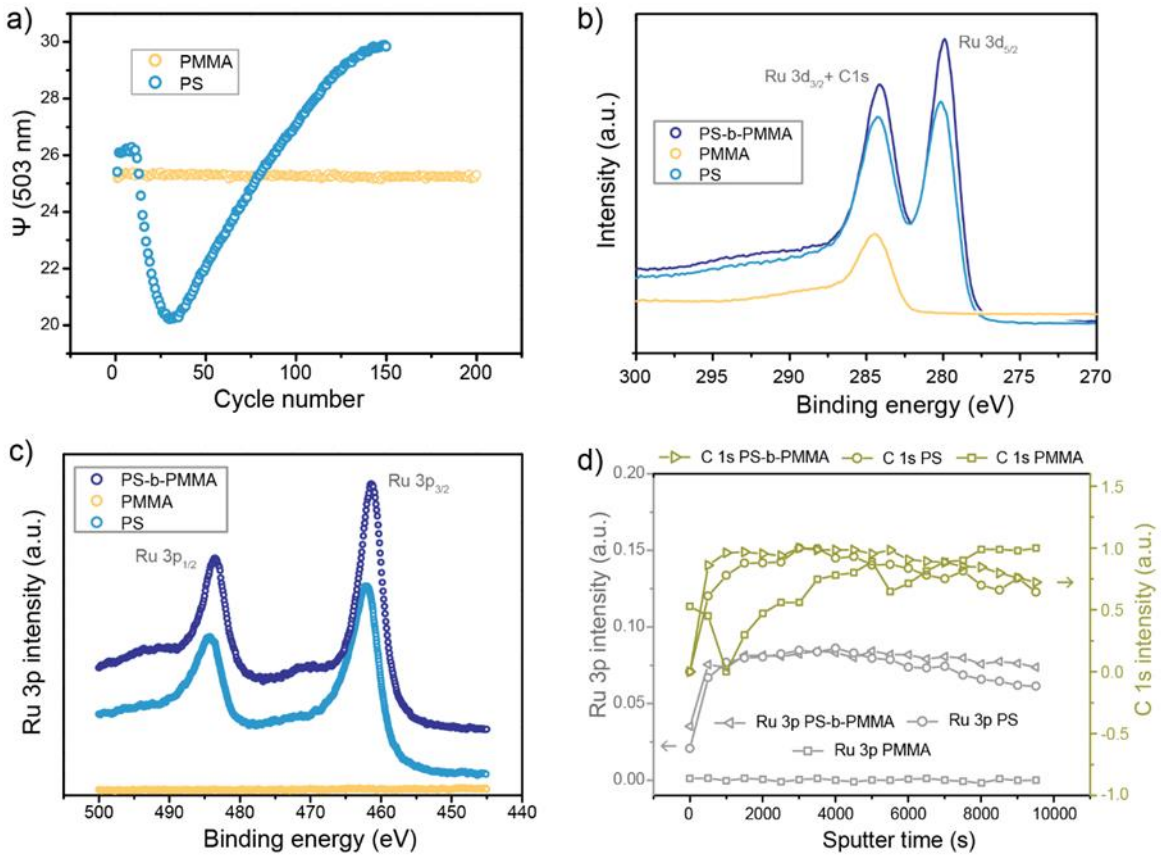

Figure 2: a) *In situ* ellipsometry data on PS and PMMA homopolymers during the Ru SIS experiments. *Ex situ* XPS after 30 SIS cycles **b)** Ru 3d peaks on PS,PMMA and PS-b-PMMA, **c)** Ru 3p peaks, **d)** XPS depth profile for C1s and Ru 3p intensities on the polymers after 30 SIS cycles.

2.2. Kinetics of RuO_4 infiltration

The uptake of RuO_4 in the polymers and potential out-diffusion profiles were studied using *in situ* spectroscopic ellipsometry (SE). We purposely designed an experiment where different

steps are coloured differently as shown in **Figure 3**. The first step of this experiment was the introduction of RuO_4 molecules (at ca. 2 mbar) to all the three polymers (i.e., PS, PMMA, and PS-b-PMMA) used in this study. Note that between subsequent RuO_4 exposures, the chamber was pumped down to the base pressure (ca. $2*10^{-6}$ mbar) and an SE measurement was taken. The red circles in **Figure 3** indicate such measurements. The change in thickness of the polymer after the precursor exposure allows to identify the swelling of the polymer caused by the precursor infiltration.[55-56] The infiltrated precursor molecules can get trapped inside the polymer, either by physical entrapment or by chemical reaction with polymer functional groups/reactive sites. Sometimes the entrapment of the precursor molecules inside the polymer is reversible leading to the polymer returning back to its original state. To get insights into such possible out-diffusion of entrapped RuO_4 molecules, the polymer thickness was probed again after a long waiting time of ca. 28 minutes. The ellipsometry measurement after this waiting time is indicated as a blue square in the figure. In the case of PMMA films (**Figure 3a**), there is no significant thickness increase after the RuO_4 exposure pulses, suggesting low uptake of RuO_4. This can be because of two reasons; either the RuO_4 molecules do not infiltrate into PMMA, or the infiltrated molecules (completely) out-diffuse in the timeframe of the pumping step. The low uptake could be related to the low solubility and (or) diffusivity of RuO_4 molecules in PMMA. On the other hand, in the case of PS (**Figure 3b**), it is quite evident that after the RuO_4 only pulse (red circles), the polymer thickness increases significantly during the initial pulses and show saturation behaviour after 20 pulses (around 20 % increase). This swelling followed by saturation is typical for infiltration reactions. Before the next SE measurement (blue square), a long waiting time of ca. 28 minutes is introduced (without pulsing any RuO_4) to reveal the potential out-diffusion of precursor from the polymer, and thus the strength of the bond formed between the RuO_4 and PS. Previous reports on trimethyl aluminium (TMA) infiltration into PMMA, one of the best studied SIS processes in literature, revealed the out-diffusion of TMA molecules after waiting for a certain time after the TMA pulse.[55] This was attributed to the relatively weak bond formed between PMMA and TMA. By contrast, in our case, even after ca. 28 minutes of waiting after the RuO_4 pulse, no significant change in thickness (decrease) was observed, indicating permanent or at least strong bonding of RuO_4 with the PS films. Further RuO_4 pulses (red circles followed by the first blue square, data from ca. 100-135 minute in Figure 3b) resulted in limited infiltration (no significant thickness increase), as now the free volume of the polymer is filled with RuO_4 molecules and thus further in-diffusion of RuO_4 is hindered. When a complete SIS cycle (RuO_4-H_2, indicated by green triangles) is performed the thickness seems to decrease as H_2 is expected to reduce the infiltrated RuO_4 (RuO_x) to Ru. Similar experiments on PS-b-PMMA (**Figure 3c**) indicate swelling (19 % after 20 RuO_4 pulses) and saturation behaviour indicating the infiltration of RuO_4 into the PS component in PS-b-PMMA films. The processing conditions and nature of

the polymer can still be tweaked to increase the free volume and hence the swelling percentage/ infiltration depth.

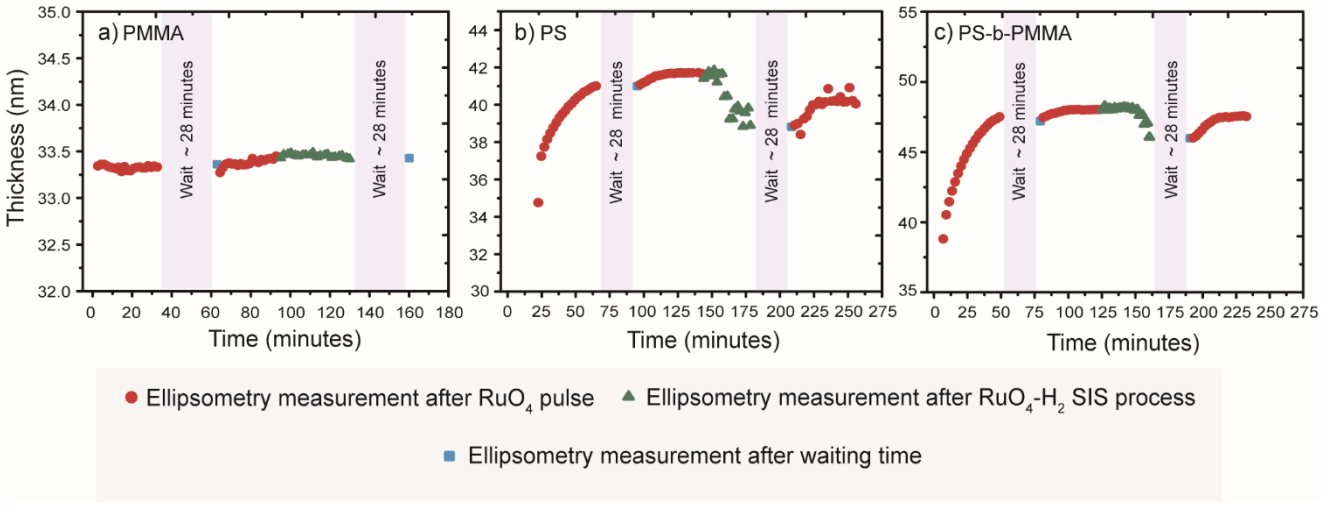

Figure 3: a),b), and c): *In situ* ellipsometry experiments on PMMA, PS and PS-b-PMMA during RuO_4 only pulses and RuO_4-H_2 process. Note the waiting time of ca. 28 minutes in the graphs The RuO_4 pulse (red dots) was introduced at ca. 2 mbar and was followed by a pumping step to reach the base pressure before an ellipsometry measurement is performed (red circles).

2.3. Crystalline nature of infiltrated Ru

The crystalline nature of the infiltrated Ru inside the PS-b-PMMA was investigated using synchrotron based GIWAXS. A series of PS-b-PMMA samples were exposed to different cycles of the Ru SIS process and these samples were then subjected to plasma treatment to remove the polymer components. Figure 4a depicts the 2D GIWAXS images for the PS-b-PMMA reference (left), after 20 SIS cycles on PS-b-PMMA (middle) and after 20 SIS cycles followed by the plasma (right). The reference PS-b-PMMA did not give rise to any scattering ring in the GIWAXS image. However, the sample after 20 SIS cycles clearly shows scattering rings typically for Ru hexagonal closed packing (hcp) structure at q_r values of ca. 26.4 nm^{-1} (100) and 30 nm^{-1} (101). For the sample after 20 SIS cycles and H_2 plasma treatment (to

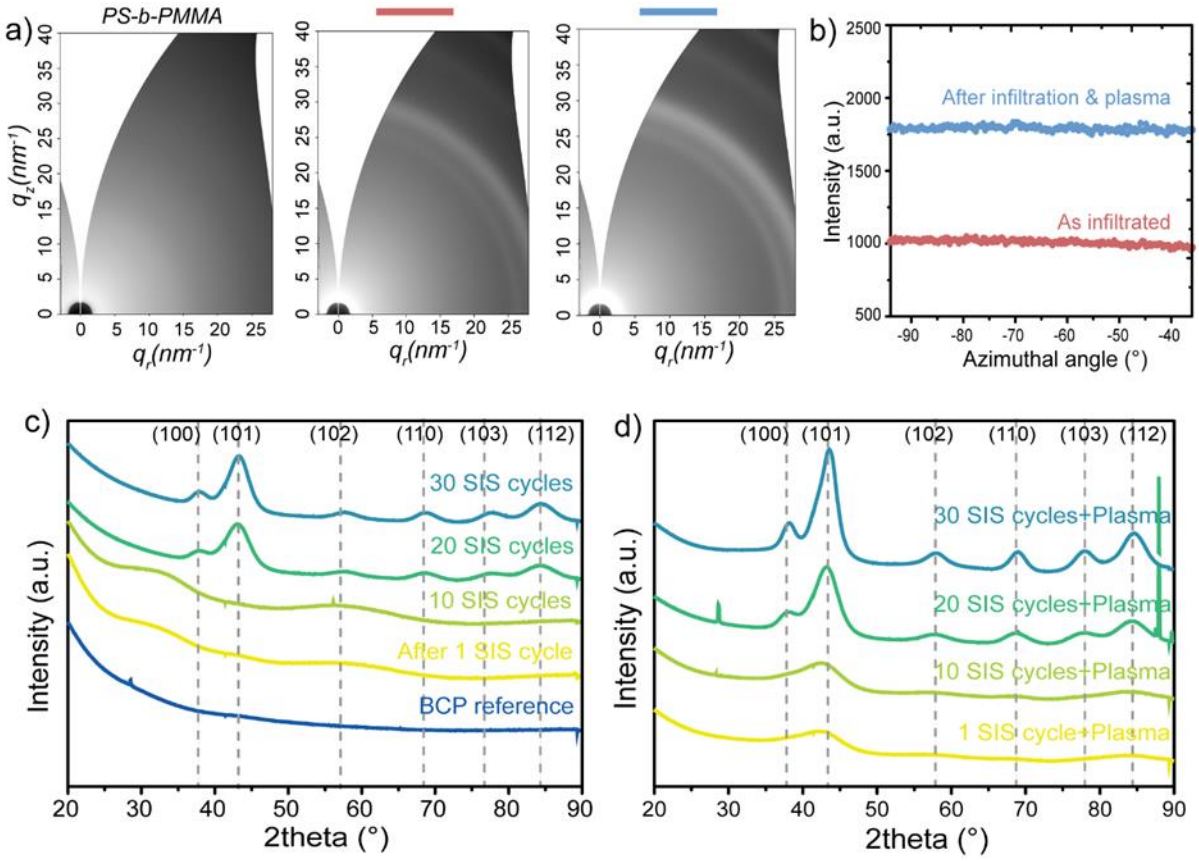

Figure 4: a) 2D GIWAXS patterns of the reference PS-b-PMMA (left), after 20 SIS cycles (middle) and after 20 SIS cycles and plasma treatment (right) **b)** Intensity vs azimuthal angle plot showing there is no anisotropic scattering from the Ru layer, **c) and d)** 1D azimuthal integration plots obtained from GIWAXS data, showing the crystalline nature of Ru inside the polymers for the as-infiltrated samples and the samles after infiltration followed by H_2 plasma treatment, respectively.

remove the organic part), the scattering ring is still present but noticeably with a higher intensity. These scattering rings shed light towards the crystalline nature of Ru present inside the polymer. The intensity profile along the peak azimuthal position does not change with the azimuthal angle (Figure 4b), proving the Ru isotropic crystallographic orientation inside the polymer for both the as-infiltrated and after plasma treated samples. However, the intensity after the plasma is substantially higher than compared to the as-infiltrated sample indicating higher crystallinity for the former set of samples. The azimuthal integration of the data thus leads to a 1D plot as shown in Figure 4c (as infiltrated) and Figure 4d (after infiltration followed by H_2 plasma).

After 20 SIS cycles (as-infiltrated), the typical diffraction patterns corresponding to Ru HCP start to appear with the peak at 43°(corresponding to the 101 plane) being the strongest in intensity. The other typically diffraction planes for Ru HCP such as 100, 102, 110, 103, 112 are also observed. Interestingly, for the sample set after the infiltration followed by plasma,

the diffraction patterns corresponding to Ru HCP start to appear even for the '1 SIS cycle plasma' sample. This enhanced crystallinity after the plasma treatment is attributed to the removal of carbon (polymeric components) from the film and the possible further reduction of any ruthenium oxide (RuO_x) present in the samples to metallic Ru during the H_2 plasma step. A similar observation of increase in crystallinity after the removal of polymer was observed during the SIS of In_2O_3 in PMMA.[57] As shown in **Figure 4c** and **4d** respectively for both as-infiltrated and after plasma samples the intensity of the peaks increased as a function of increase in SIS cycles as expected due to the increase in Ru loading.

2.4. Morphological Analysis

The morphological evaluation of the infiltrated polymers was carried out using SEM, AFM, and GISAXS measurements. The SEM images 'after infiltration' and 'after infiliration followed by plasma' are provided in Figure S4 and S5, respectively. Topograhical AFM images in **Figure 5a** reveal the fingerprint self-assembly of the reference di-BCP films (indicated as 0 SIS cycle). However, in this case the contrast between the PS and PMMA domain in the pristine film is poor. After the Ru SIS cycles, a significant enhancement in morphological contrast between the two domains of the di-BCP is observed, which suggests the selective incorporation of Ru into one of the domains. Based on the previously discussed ellipsometry and XPS data, this domain likely corresponds to the PS domain. Notably the contrast increases as a function of Ru loading (increase in SIS cycles). Interestingly, a single SIS cycle itself already results in an enhanced contrast implying that there is Ru present in the di-BCP after just 1 cycle. The formation of Ru nanopatterns after the H_2 plasma treatment to remove the polymer layer, mimicking the original di-BCP pattern is also verified (Figure 5b). A reference sample (Figure 5b, labelled as '0 SIS cycles') was also exposed to the H_2 plasma treatment, and the AFM image of this sample revealed the absence of any features on the surface compared to the pristine PS-b-PMMA. This means the plasma condition used here is able remove most of the organic components. However, it is unclear whether all the organic components are removed from the infiltrated PS domains after the plasma treatment, and the analysis of this is difficult using XPS due to the overlap of C 1s with Ru 3d. The indication of the original fingerprint pattern on the sample 'after 1 SIS cycle and plasma' confirms the presence of Ru inside the template just after 1 SIS cycle.

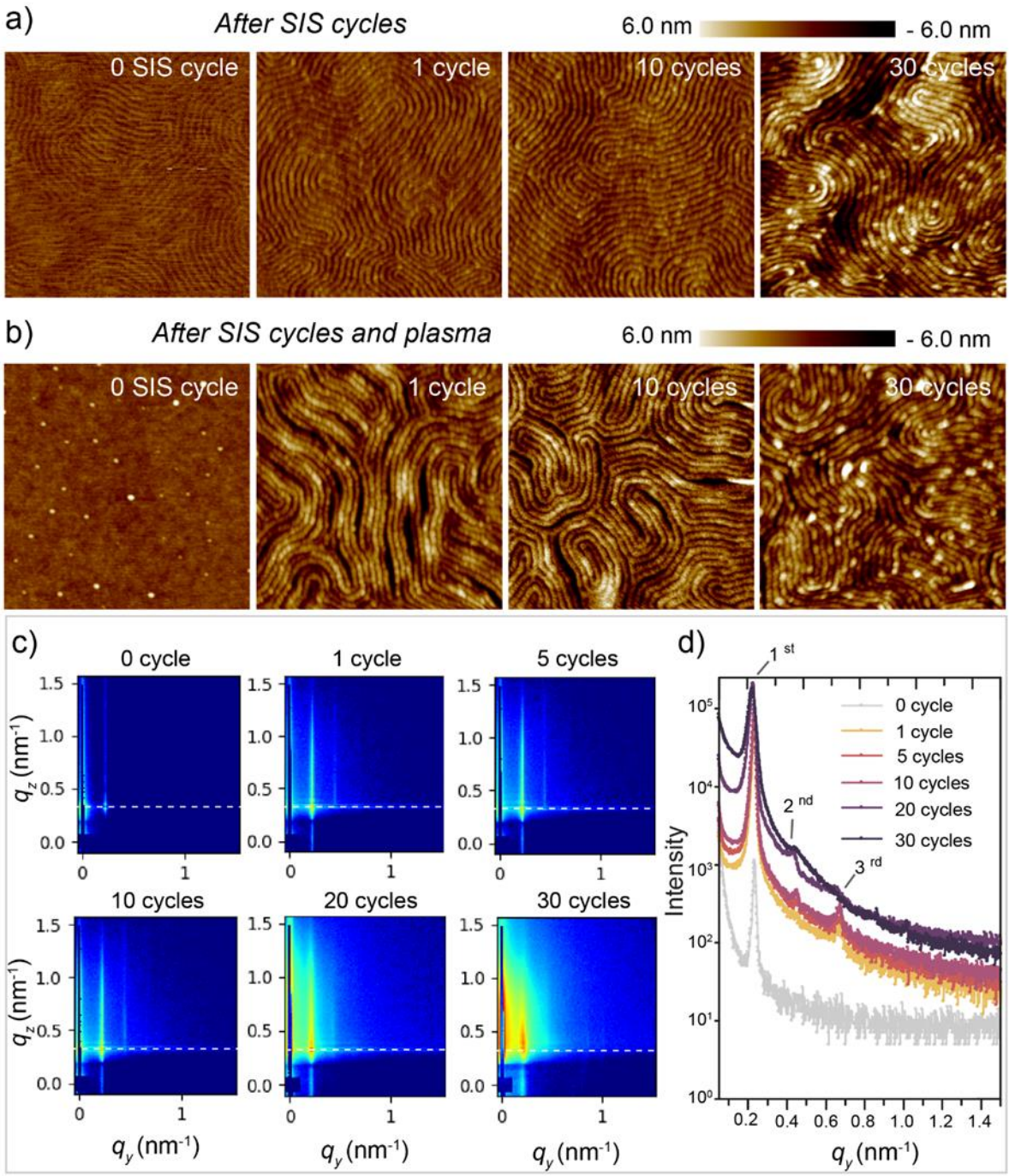

Figure 5 : Topographical AFM images a) as-infiltrated, b) after infiltration followed by H_2 plasma. The sides of the square indicate 500 nm. c) 2D GISAXS images of the as-infiltrated samples and d) 1D horizontal line profiles for the as-infiltrated samples taken at q_z = 0.45 nm^{-1} (dashed lines in C)).

Complementary GISAXS measurements were performed to further analyse the morphological evolution of the as infiltrated samples as a function of SIS cycles. As seen from the 2D GISAXS images in Figure 5c, the pristine di-BCP film gave rise to a first order interference peak at a q_y

position of 0.23 nm^{-1}. This implies that the polymer domains are laterally ordered with an average spacing of ca. 27 nm, which was calculated using the approximation d=2π/q, q being the q_y peak position. Also, after the first SIS cycle, results in an immediate increase in the intensity of first-order scattering peak and development of a second-order peak at ca. 0.46 nm^{-1} and a third-order peak at 0.67 nm^{-1}. This reveals an excellent registry of the Ru incorporation within the di-BCP template, in agreement with the AFM data.[58] In general, addition of Ru to the polymer increases the diffuse scattering in the GISAXS images and this is found to follow an increasing trend with respect to the number of cycles. As seen from the 1D cuts in Figure 5d, the q_y position (0.23 nm^{-1}) after the infiltration cycles tend to remain more or less the same compared to the original di-BCP, corroborating the templated Ru deposition. At higher SIS cycles, for example 20 and 30 SIS cycles, the q_y position slightly shifts to slightly lower q_y values, possibly because of the increased diffuse scattering from the Ru nanoclusters. After 20 SIS cycles, the possibility of a quasi-uniform thin Ru layer on top of the polymer film can also not be excluded. To conclude the discussion on the AFM and GISAXS data, there is templated incorporation of Ru inside the di-BCP template, which increases as a function of SIS cycles, under the conditions studied. Based on the results obtained from in situ ellipsometry and XPS, the increase in contrast and templated growth of Ru nanostructures is attributed to the selective growth in PS domains.

2.5. Mechanism of Ru infiltration

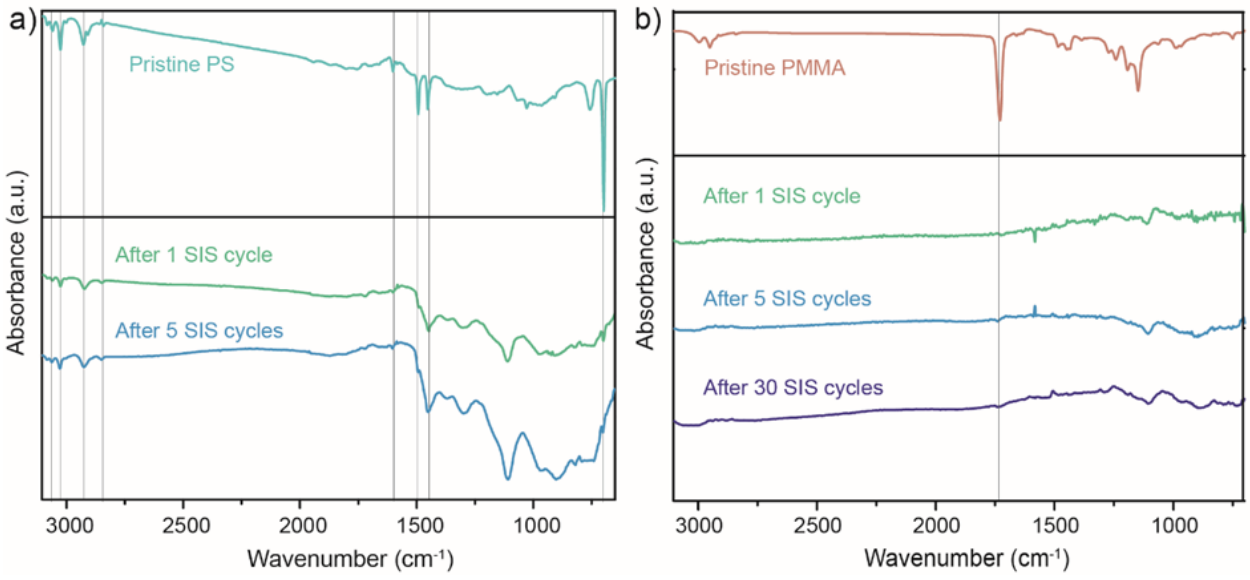

Figure 6: *In situ* FTIR data during RuO_4 infiltration on PS and PMMA blanket homopolymers. a) on PS, b) on PMMA. The reference spectra of the polymer films are shown on top of the graphs. The *in situ* spectra during the SIS process were recorded, and then subtracted from the spectrum recorded for the corresponding polymer film on Si to obtain difference spectra.

In situ FTIR spectroscopy was used to analyse the chemical groups that are removed or introduced during the Ru SIS process. To this end, the interaction of RuO_4 with PS and PMMA blanket films were monitored using FTIR. First, the reference spectra for the polymer layers were recorded by subtracting the spectrum for a blanket Si wafer from the recorded data. Afterwards, *in situ* measurements were carried out, recording the spectra, and then subtracting the spectrum recorded for the polymer film on Si to obtain difference spectra. Hence, during the *in situ* process, the positive features indicate the chemical groups that are formed and the negative features account for the groups that are being consumed during the reaction.

The PS and PMMA spectra (referenced to the blank Si substrate) are provided in **Figure 6a and b** for easy comparison. The features associated with the blanket homopolymers, and their corresponding assignments are provided in **Table S1**. After the RuO_4 pulses, as evident from **Figure 6a**, negative features appear around 3026 cm^{-1}, 3063 cm^{-1} , and 3082 cm^{-1}, which reveals the interaction and subsequent consumption of aromatic CH groups by the RuO_4 molecules. Another set of negative features, that appear around 1602 cm^{-1}, 1584 cm^{-1}, 1493 cm^{-1}, and 1452 cm^{-1} correspond to aromatic C=C/C-C stretching. These features become more evident with higher SIS cycles (5 cycles as shown in Figure 6a). The other weak features that get consumed are around 2926 cm^{-1}, 2847 cm^{-1} (asymmetric, symmetric stretching of methylene, $-CH_2$, respectively), and the out of plane CH bending at ca. 698 cm^{-1}. There is a sharp dip to be seen around 1100 cm^{-1}, which is clearly not related to the peak from the pristine PS sample. This peak has been previously attributed to Si-O-Si bond.[59] The decrease in intensity of this peak is likely due to the diffused RuO_4 molecules interacting with the Si substrate underneath the polymer film. Indeed, additional *in situ* measurements (**Figure S6**) during RuO_4 exposure on a Si sample (without the polymer) also indicated that this peak intensity decreases during RuO_4 pulses. However, in general the interaction and consumption of aromatic C-H and C=C groups by RuO_4 even after just 1 RuO_4 pulse, is clear from the *in situ* FTIR data, in agreement with other data presented before.

On the other hand, the blanket PMMA spectrum (**Figure 6b**) indicates the typical feature expected for the C=O group at 1730 cm^{-1} as the major peak (other peak assignments are provided in the supporting information). The spectrum after 5 RuO_4 pulses and even after 30 RuO_4 pulses did not lead to significant changes compared to the pristine PMMA spectrum, indicating the absence of (significant) interaction of RuO_4 with PMMA related groups, in agreement with all other data presented earlier. Therefore, in summary the interaction of RuO_4 molecules with PS happens from the first cycle onwards, via the consumption of aromatic C-H and C=C species present in the polymer, while with PMMA the lack of such chemical groups means that the interaction with RuO_4 is limited.

Density functional theory (DFT) calculations were performed to investigate the interactions of the RuO_4 precursor and the PMMA and PS oligomers during the SIS process. **Figure 7** shows the relaxed atomic structure of PMMA after the interaction with one RuO_4 molecule. We have considered two different interaction sites of PMMA. In the first model the RuO_4 molecule was placed between the monomer units and near the methoxy group of PMMA while in the second model the RuO_4 molecule was placed near the methyl group of PMMA. The optimised atomic structures show that no new bonds are formed between PMMA and RuO_4. The calculated interaction energies for the first model (**Figure 7a1**) and the second model (**Figure 7a2**) are 0.27 eV and -0.05 eV, respectively and these show an unfavourable interaction between RuO_4 and PMMA. This is consistent with findings from FTIR, which show the chemical groups associated with PMMA were not affected during the RuO_4 pulse. The lack of interaction between RuO_4 and PMMA can contribute to the low infiltration of RuO_4 into PMMA, while the low solubility and/or low diffusivity of RuO_4 in PMMA may also play a role, as explained before.

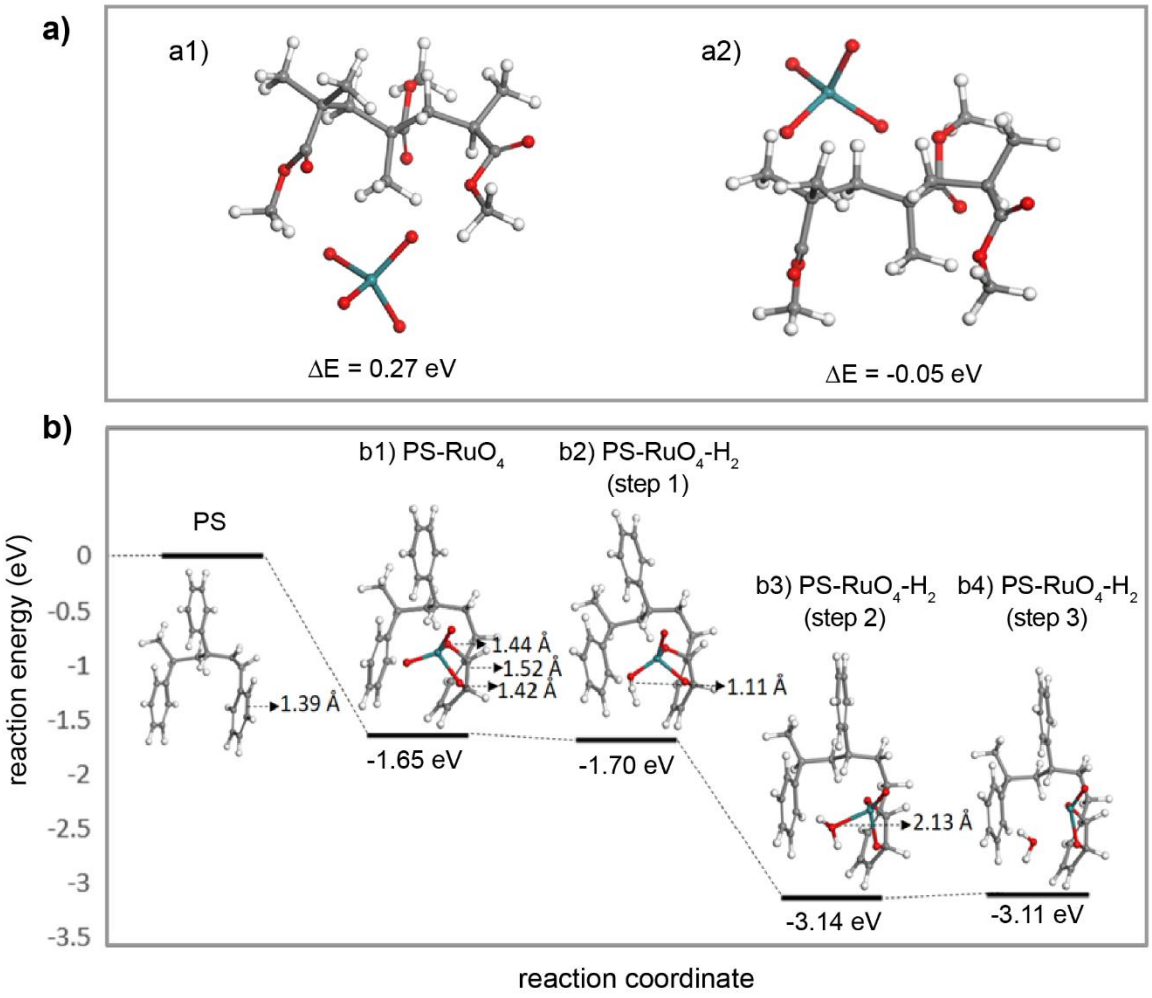

Figure 7: a) Optimised atomistic structure of RuO_4 located **a1)** near the methoxy group of PMMA, **a2)** near the methyl group of PMMA. **b)** The plotted reaction pathway of PS polymer with the metallic precursor RuO_4 and co-reactant H_2. Optimised atomistic structures of **b1)** PS interacting with RuO_4, **b2)** PS interacting with RuO_4 and H_2, **b3)** PS interacting with RuO_4 and H_2-H_2O formation, **b4)** PS interacting with RuO_4 and H_2-H_2O release. Grey-carbon, red-oxygen, white-hydrogen, blue-ruthenium.

The optimised atomic structure of PS after the interaction with one RuO_4 molecule presented in **Figure 7b1**, shows that RuO_4 binds to the aromatic C atoms of PS by forming two new O-C bonds with distances 1.44 Å and 1.42 Å. After binding with RuO_4, the C-C distance of these C atoms increases from 1.39 Å in PS to 1.52 Å, which removes the aromatic character of the ring. The calculated interaction energy, -1.65 eV, indicates an exothermic interaction, and therefore the interaction is favourable. This is in line with findings from FTIR, which show that after the RuO_4 pulse aromatic C=C bonds of PS polymer are consumed. The findings from *in situ* ellipsometry also indicate a strong bonding of RuO_4 with the PS films.

Next, to investigate interactions between RuO_4-PS and H_2 (co-reactant) we expand the RuO_4-PS model to include one H_2 molecule. **Figure 7b2** depicts the optimised atomic structure of RuO_4-PS after the incorporation of one H_2 molecule. The H_2 molecule binds with one O atom of RuO_4 with a H-O distance 1.11 Å. The overall calculated energy change for this reaction is -1.70 eV. In the next step we consider the formation of one H_2O molecule. The optimised atomic structure of this reaction product is presented in **Figure 7b3**. This reaction involves the dissociation of the H_2 molecule and the binding of the H atoms with one O atom of RuO_4 to form a H_2O molecule while the existing Ru-O bond is lengthened from 1.65 Å to 2.13 Å. The calculated energy gain for this reaction is -1.44 eV relative to the model in **Figure 7b2**, leading to an overall energy change of -3.14 eV. The final step of H_2 and RuO_4-PS involves breaking the existing Ru-O bond and the release of a H_2O molecule. The optimised atomic structure of this reaction product is presented in **Figure 7b4** and the calculated energy cast to release a H_2O molecule is 0.03 eV relative to the model in **Figure 7b3**, leading to an overall energy change of -3.11 eV. The negative energies calculated for the reactions of RuO_4-PS with H_2 indicate that H_2 co-reactant is able to reduce the RuO_4 molecules infiltrated into the PS polymer, consistent with formation of metallic Ru.

2.6. SIS of RuO_2 nanostructures

In this work, we have shown that Ru nanopatterns can be achieved by the selective infiltration of RuO_4 into PS domains of PS-b-PMMA. Next, we show that RuO_2 nanostructures can also be accomplished by SIS, utilizing a RuO_2 ALD process that uses the same Ru source (RuO_4)

but employs alcohols as co-reactants (Figure 8a). The details of the ALD process are presented elsewhere.[60] Specifically, RuO_4 and methanol (the growth per cycle of this process is around 1 Å/cycle) were used as reactants for RuO_2 SIS at a substrate temperature of 120 °C. 50 cycles of this process were done on blanket PS, PMMA, and PS-b-PMMA di-BCP thin films to evaluate the selectivity of this process. A higher number of SIS cycles was presented in the manuscript for the RuO_2 SIS process to show that the selective reaction towards polystyrene is not lost even after 50 SIS cycles. XPS (Figure 8b) measurement on PS after RuO_2 infiltration (50 cycles) shows the presence of Ru 3p peaks, whereas no peak was present on PMMA blanket films. As a result, the selective nature of the RuO_2 SIS process is confirmed,

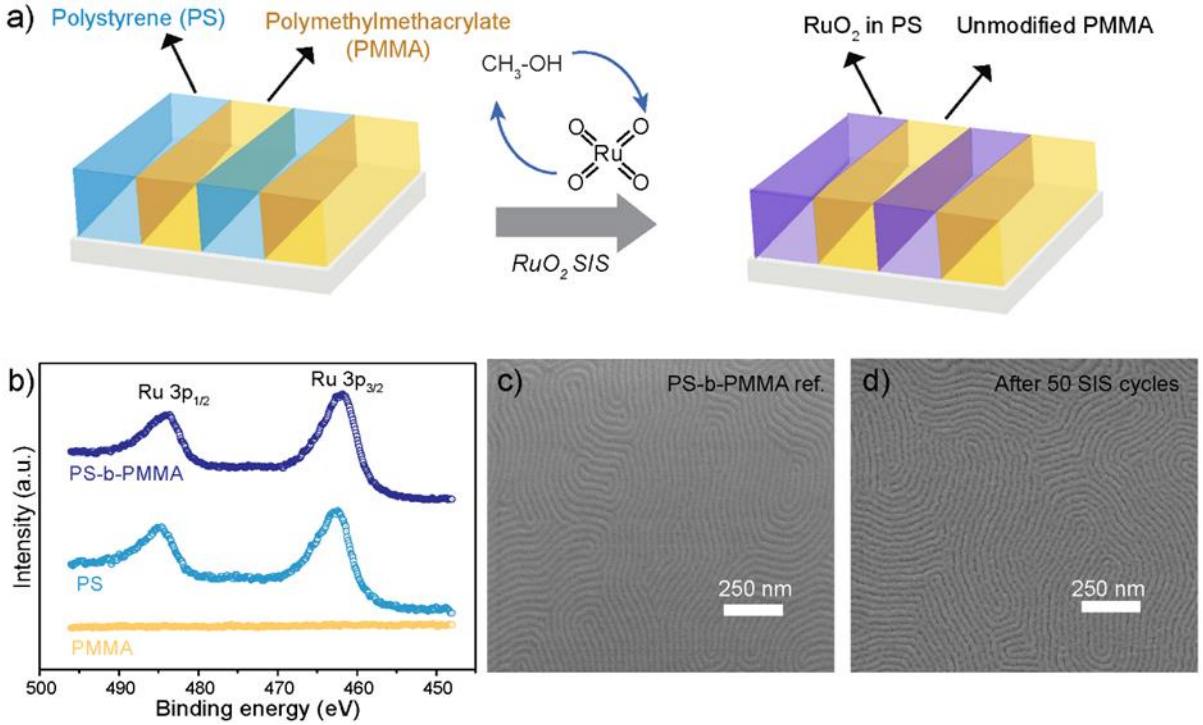

just as it was for the Ru process. PS-b-PMMA, as expected, produced a Ru peak in XPS, identical to that seen for PS. Moreover, we confirmed the presence of Ru in PS blanket samples using energy dispersive X-ray analysis (data not shown), after performing lower number of SIS cycles as well (10 cycles).

Figure 8: RuO_2 SIS using methanol-RuO_4 ALD process. **a)** Schematic illustration of the SIS of RuO_2 on PS-b-PMMA **b)** Ru 3p XPS spectra after 50 SIS cycles of methanol-RuO_4 ALD process at a substrate temperature of 100°C. All the polymers were around 30-35 nm thick. **c)** SEM image of pristine polymer film and **d)** the same film after 50 RuO_2 SIS cycles.

To verify that it is indeed RuO_2 that is being infiltrated into the PS domains, when using the RuO_4-methanol SIS process, we performed additional *in situ* XRD characterization (**Figure**

S7). The samples after 50 SIS cycles were annealed in He atmosphere to 500 °C. From the *in situ* XRD plot, it clear that a peak (at around 28°) corresponding to RuO_2 (110) plane starts to appear around 240 °C. This confirms that the infiltrated material is indeed, RuO_2, but present in amorphous form in the as-infiltrated samples. On the other hand, as expected for the RuO_4-H_2 SIS process, there was no peak corresponding to RuO_2, but a clear peak corresponding to metallic Ru (101) was present.

This indicates that the PS-b-PMMA di-BCP can be used to generate RuO_2 nanopatterns on the surface, with RuO_2 mimicking the reactive PS component of the block copolymer. Figure 8c shows the SEM image of PS-b-PMMA, which shows the lamellar self-assembly of the PS and PMMA blocks. The SEM image of the polymer thin film after 50 SIS cycles (**Figure 8d**) clearly reveals an increase in contrast when compared to the pristine polymer thin film, implying RuO_2 infiltration. Exposure times, number of SIS cycles, and other variables can still be tweaked to improve infiltration depth and RuO_2 pattern dimensions. The diverse morphologies offered by the self-assembly of the blocks in the block-copolymer in combination with SIS might yield potential nanostructures, such as Ru and RuO_2, as shown here.

3. Conclusions and outlook

We have established a new sequential infiltration synthesis (SIS) procedure for ruthenium metal nanostructures, primarily with the goal of expanding the SIS library to metal nanostructures without the requirement for any pre-treatment. The SIS approach is based on a previously described ALD process for Ru, in which RuO_4 is the Ru source and H_2 is the co-reactant. We demonstrated selective infiltration of RuO_4 within PS blanket homopolymer films, whereas no reaction was observed with PMMA thin films, as evidenced by XPS, SE, and FTIR. Self-assembled PS-b-PMMA films were then used to create Ru nanostructures that mimicked the reactive PS component. AFM and GISAXS images displayed an increased contrast as a function of Ru loading in the polymer. The templated deposition of Ru in the di-BCP was confirmed from these measurements. The increased contrast and templated deposition are very likely related to the selective interaction between PS and RuO_4 in the di-BCP, judging from the XPS and ellipsometry data on blanket polymers. GIWAXS indicated that the as-infiltrated PS-b-PMMA and Ru nanostructures obtained after plasma treatment exhibited a quasi-isotropic crystal structure. However, when compared to the as-infiltrated samples, the crystallinity of Ru nanostructures improved even more when the polymer was removed. *In situ* FTIR analysis revealed that polystyrene's aromatic C=C and CH bonds are consumed during the process, but no chemical groups linked with PMMA were disturbed. This was backed up by DFT calculations which corroborated the observed selectivity difference. The unfavourable

interaction of PMMA with RuO4 could be related to the low solubility and (or) diffusivity of RuO_4 in PMMA. DFT studies also show that the co-reactant H_2 is able bind to oxygen in RuO_4, allowing the formation of metallic Ru with the release of H_2O. We also show that RuO_2 nanopatterns can be achieved using the same di-BCP by modifying a RuO_2 ALD process that uses RuO_4 and alcohols as reactants.

With the growing interest in metals such as Ru, Co, and others in microelectronics, SIS could be a useful technique for creating possible nanostructures of these metals without the need for complicated lithographic procedures. The diverse library and versatility of block copolymers in self-assembly, along with successive infiltration of ALD precursors, opens up a world of possibilities for next-generation metal (oxide) nanopatterns in a variety of applications. For instance, SIS has already been successful for the creation of ZnO/Al_2O_3 nanostructure arrays by carefully controlling the diffusion times of the precursors involved.[61] Similarly, the work presented in this manuscript can potentially be extended to the synthesis of different metal/dielectric nanostructures starting from a single di-BCP (PS-b-PMMA for example). The well-studied Al_2O_3 SIS process has been already shown to selectively occur preferentially in the PMMA domains, leaving the PS domains inert. On the other hand, the Ru SIS process demonstrated in this work is selective towards PS, without modifying the PMMA part. In principle, these two SIS processes could be performed one after the other on a PS-b-PMMA template. In this way, the different domains of the BCP are decorated with a metal and a dielectric material by combining two separate SIS processes (Ru and Al_2O_3 for instance). Removing the polymer template thus allows for the fabrication of periodic metal/dielectric nanopatterns. This concept would not only allow for the direct synthesis of metal/dielectric patterns with tuneable morphologies based on the original BCP, but it would also reduce the complexity associated with the synthesis of such structures using traditional methods. Similarly, by carefully identifying suitable precursors that preferentially react with one of the blocks of the (di-, tri-) BCP, the distinct chemical character of the domains in different BCPs could be exploited to generate alternative functional nanostructures (metal/metal, metal/metal nitrides, etc.).

4. Materials and Methods

4.1. . Block copolymer film preparation

PS-*b*-PMMA film was prepared using the 300 mm wafer process at imec. A neutral brush (PS-*ran*-PMMA brush, AZEMBLY NLD-127) was first coated on bare Si wafer. After annealing at 250^{o}C for 5 min, non-grafted excess brush was rinsed with solvent (1-Methoxy-2-propanol acetate; propylene glycol monomethyl ether acetate (PGMEA)), resulting in 5 nm-thick neutral brush grafted on a Si wafer. 35 nm-thick lamellar-forming PS-*b*-PMMA was then spin coated

and annealed at 250°C for 5 min under N_2 environment. Further details on the BCP preparation are described elsewhere.[62] Prior to the infiltration experiments the polymer samples were heated in vacuum at 100°C for half an hour to remove any residual solvents or adsorbed moisture from the films. Prior to the infiltration experiments the polymer samples were heated in vacuum at 100°C for half an hour to remove any residual solvents or adsorbed moisture from the films.

4.2. Sequential infiltration synthesis

All the SIS processes of Ru and RuO_2 were performed in a custom-built ALD reactor reported elsewhere.[63] The reactor is equipped with a turbomolecular pump with a gate valve, such that a base pressure of ca. 10^{-6} mbar is achieved. The sample is heated inside the chamber with a resistive heater. It is to be noted that in this work, not pure RuO_4, rather a solution of RuO_4 in a methyl-ethyl fluorinated solvent (ToRuS) developed, produced, and supplied by Air Liquide was used as the Ru source for the infiltration experiments. The concentration of RuO_4 in the solution is very low (less than 1%) such that if there are spills, the danger is limited. Moreover, no evidence of toxicity was found in the ToRuS solution as a result of an inhalation study conducted by Air liquid. Nevertheless, the use of personal protection equipment, including respiratory protection methods (ABEK2 filters) is strongly advised.[64] H_2 gas was supplied by using a 20% mixture of H_2 in Ar. The substrate temperature was kept at 120 °C. For Ru SIS, the previously reported RuO_4-H_2[49] ALD process was modified. Both RuO_4 and H_2 pulses were static in nature. That is, the valve between the chamber and the turbo pump was closed to allow the pressure to build up by injecting the gas over a time, t_i. After this, the pneumatic inlet was closed and thereby allowing the chamber to remain at a constant pressure P_s for a time t_s. The chamber was pumped down to a pressure of about 10^{-1} mbar with the rotary pump before opening the valve to the turbo pump again, reaching a base pressure of 10^{-6} mbar. The values for {P_s, t_i, t_s} for the RuO_4 and H_2 gas pulses were {2 mbar, 20 s, 50 s} and {5 mbar, 20 s, 20 s}, respectively. For the RuO_2 SIS process, the methanol-RuO_4 ALD process was used. Both methanol and RuO_4 pulses were again static in nature with {P_s, t_i, t_s} equal to{1 mbar, 40 s, 10 s} and {1 mbar, 20 s, 10 s} for the RuO_4 and methanol pulses, respectively.

4.3. Characterization techniques

In situ spectroscopic ellipsometry (SE) during the infiltration was performed with a SE, J. A. Woollam M – 2000 with a wavelength from 245 to 1000 nm. A Cauchy model was applied for fitting the ellipsometry data. X-ray fluorescence (XRF) measurements were performed by using a Mo X-ray source (at an angle of 45° with the sample surface) and a silicon drift detector that is placed at an angle of 52° with the sample surface. The fluorescence signal was

integrated over a period of 100 s. X-ray photoelectron spectroscopy (XPS) measurements were performed on a Thermo Scientific Theta Probe XPS instrument using Al Kα (λ =0.834 nm) X-rays generated at 15 kV and 70 W and focused to a spot size of 0.3 mm by an MXR1 monochromator gun. As the Ru 3d region overlaps with C 1s, we used the Ru 3p region to detect ruthenium in the polymer films. The acquired data was analyzed using the CasaXPS software package. The *in situ* infrared measurements are carried out with a Vertex 70 V from Bruker and a medium band mercury cadmium telluride (MCT) detector cooled with liquid nitrogen. The data was analyzed using OPUS software provided by Bruker.

Scanning electron microscopy (SEM) measurements were performed on a FEI Quanta 200F and a FEI Sirion instrument. Atomic force microscopy (AFM) measurements were done on a Bruker Dimension Edge system operating in tapping mode in air. Grazing incidence small angle X-ray scattering (GISAXS) and grazing incidence wide angle X-ray scattering (GIWAXS) experiments were performed at the NCD-SWEET beamline of the ALBA synchrotron, Spain. The X-ray beam energy was set to 12.4 keV using a Si (1 1 1) channel cut monochromator and further collimated with an array of Be lenses. Two area detectors were used, being the Pilatus3 S 1M for GISAXS and Rayonix LX-255HS for GIWAXS. The incident angle was set at 0.15° which is well above the critical angle of PS-b-PMMA but below the critical angle of the substrate for the employed energy. The scattering vector $\vec{q}$ was calibrated by using silver behenate and chromium trioxide as reference standards, obtaining a sample to detector distance of 6681 mm and 155.7 mm for GISAXS and GIWAXS, respectively.

4.4. Computational methods

Density functional theory (DFT) calculations were carried out using the TURBOMOLE suite programs.[65] The PMMA polymer model is an oligomer that consists of three methyl methacrylate monomers and the PS polymer model is an oligomer that consists of three styrene monomers, **Figure 9**. The hybrid Perdew-Burke-Ernzerhof (PBE0) functional was used for these calculations, which incorporates 25% exact HF exchange,[66] while a polarized split valance basis set, denoted def-SV(P), is used.[67] An effective core potential is used for Ru, with 28 core electrons. A fine integration grid (m3) was used and SCF convergence criterion was set to 10^{-6} Ha. Convergence criteria for the geometry was set to 10^{-3} Ha. Interaction energies were calculated using:

$E_{int} = \sum E_p - \sum E_r$

Here, E_p and E_r are the energies of products and of reactants, respectively.

For PMMA and PS polymers interacting with RuO_4:

$E_{int} = [E(RuO_4\text{-PMMA/PS})] - [E(RuO_4)+E(PMMA/PS)]$

Here, E(RuO_4-PMMA/PS) is the computed total energy of RuO_4 interacting with the PMMA or PS oligomer, E(RuO_4) is the computed total energy of the RuO_4 precursor molecule and E(PMMA/PS) is the computed total energy of the PMMA or PS oligomer.

E_{int}= [E(H_2-RuO_4-PMMA/PS)] - [E(H_2)+E(RuO_4-PMMA/PS)]

Here, E(H_2-RuO_4-PMMA/PS) is the computed total energy of H_2 interacting with the RuO_4-PMMA or RuO_4-PS, E(H_2) is the computed total energy of the H_2 molecule. A negative value for E_{int} means that the interaction is exothermic.

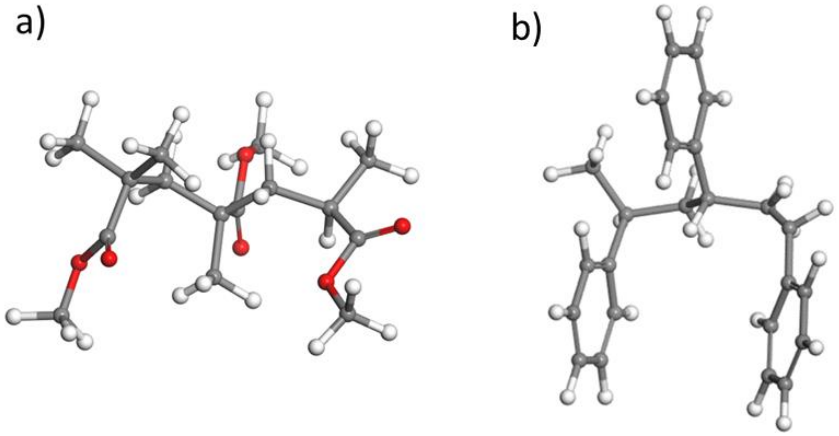

Figure 9: Optimised atomistic structure of **a)** PMMA three unit oligomer and **b)** PS three unit oligomer. Grey-carbon, red-oxygen, white-hydrogen.

ASSOCIATED CONTENT

Supporting Information

XRF spectra on PS, PMMA and PS-b-PMMA indicating selective infiltration, complete set of 2D GIWAXS images after infiltration and after infiltration followed by plasma. SEM images after infiltration, FTIR peak assignments for pristine PS and PMMA. XPS analysis strategy.

AUTHOR INFORMATION

Corresponding Author

*Email: Jolien.Dendooven@UGent.be

Conflicts of interest

There are no conflicts of interest to declare.

Author Contributions

The manuscript was written through contributions of all authors. All authors have given approval to the final version of the manuscript.

Notes

The authors declare no competing financial interest.

Acknowledgements

This project has received funding from the European Union's Horizon 2020 research and innovation program under the Marie Skłodowska-Curie grant agreement no. 765378. The authors would like to acknowledge Air Liquide for supplying the ToRuS precursor. The Special Research Fund BOF of Ghent University (GOA 01G01513) is also acknowledged. We thank Marina Baryshnikova, Pieter Vanelderen, and Hyo Seon Suh from imec for providing the polymer films. Robin Petit is acknowledged for discussions on SE and FTIR. E.S. acknowledges the Spanish project RTI2018-093996-B-C32 MICINN/FEDER funds. GISAXS and GIWAXS experiments were performed at ALBA synchrotron with the collaboration of ALBA staff. A.M. and M.N. acknowledge support from Science Foundation Ireland for computational resources at Tyndall National Institute. MN acknowledges funding from Science Foundation Ireland through the SFI-NSF China Partnership program, project NITRALD, Grant Number 17/NSFC/5279.

References

1. Aaltonen, T.; Alén, P.; Ritala, M.; Leskelä, M., Ruthenium Thin Films Grown by Atomic Layer Deposition. *Chemical Vapor Deposition* **2003**, *9*, 45-49.
2. Parkin, S.; More, N.; Roche, K., Oscillations in Exchange Coupling and Magnetoresistance in Metallic Superlattice Structures: Co/Ru, Co/Cr, and Fe/Cr. *Physical review letters* **1990**, *64*, 2304.
3. Hoefflinger, B., Itrs: The International Technology Roadmap for Semiconductors. In *Chips 2020*, Springer: 2011; pp 161-174.
4. Kil, D.-S.; Song, H.-S.; Lee, K.-J.; Hong, K.; Kim, J.-H.; Park, K.-S.; Yeom, S.-J.; Roh, J.-S.; Kwak, N.-J.; Sohn, H.-C. In *Development of New Tin/Zro2/Al2o3/Zro2/Tin Capacitors Extendable to 45nm Generation Drams Replacing Hfo2 Based Dielectrics*, 2006 Symposium on VLSI Technology, 2006. Digest of Technical Papers., IEEE: 2006; pp 38-39.
5. Wei, J.; Iglesia, E., Reaction Pathways and Site Requirements for the Activation and Chemical Conversion of Methane on Ru− Based Catalysts. *The Journal of Physical Chemistry B* **2004**, *108*, 7253-7262.
6. Cherevko, S.; Geiger, S.; Kasian, O.; Kulyk, N.; Grote, J.-P.; Savan, A.; Shrestha, B. R.; Merzlikin, S.; Breitbach, B.; Ludwig, A., Oxygen and Hydrogen Evolution Reactions on Ru,

Ruo2, Ir, and Iro2 Thin Film Electrodes in Acidic and Alkaline Electrolytes: A Comparative Study on Activity and Stability. *Catalysis Today* **2016**, *262*, 170-180.

7. Han, J. H.; Han, S.; Lee, W.; Lee, S. W.; Kim, S. K.; Gatineau, J.; Dussarrat, C.; Hwang, C. S., Improvement in the Leakage Current Characteristic of Metal-Insulator-Metal Capacitor by Adopting Ruo2 Film as Bottom Electrode. *Applied Physics Letters* **2011**, *99*, 022901.

8. Majumdar, D.; Maiyalagan, T.; Jiang, Z., Recent Progress in Ruthenium Oxide-Based Composites for Supercapacitor Applications. *ChemElectroChem* **2019**, *6*, 4343-4372.

9. Over, H., Surface Chemistry of Ruthenium Dioxide in Heterogeneous Catalysis and Electrocatalysis: From Fundamental to Applied Research. *Chemical Reviews* **2012**, *112*, 3356-3426.

10. Trasatti, S., Electrocatalysis: Understanding the Success of Dsa®. *Electrochimica Acta* **2000**, *45*, 2377-2385.

11. Dasgupta, N. P.; Lee, H.-B.-R.; Bent, S. F.; Weiss, P. S., Recent Advances in Atomic Layer Deposition. *Chemistry of Materials* **2016,** *28,* 1943-1947.

12. Cremers, V.; Puurunen, R. L.; Dendooven, J., Conformality in Atomic Layer Deposition: Current Status Overview of Analysis and Modelling. *Applied Physics Reviews* **2019**, *6*, 021302.

13. Johnson, R. W.; Hultqvist, A.; Bent, S. F., A Brief Review of Atomic Layer Deposition: From Fundamentals to Applications. *Materials today* **2014**, *17*, 236-246.

14. George, S. M., Atomic Layer Deposition: An Overview. *Chemical reviews* **2010**, *110*, 111-131.

15. Ritala, M.; Leskelä, M., Atomic Layer Deposition. In *Handbook of Thin Films*, Elsevier: 2002; pp 103-159.

16. Detavernier, C.; Dendooven, J.; Sree, S. P.; Ludwig, K. F.; Martens, J. A., Tailoring Nanoporous Materials by Atomic Layer Deposition. *Chemical Society Reviews* **2011**, *40*, 5242-5253.

17. Austin, D. Z.; Jenkins, M. A.; Allman, D.; Hose, S.; Price, D.; Dezelah, C. L.; Conley Jr, J. F., Atomic Layer Deposition of Ruthenium and Ruthenium Oxide Using a Zero-Oxidation State Precursor. *Chemistry of Materials* **2017**, *29*, 1107-1115.

18. Kwon, O.-K.; Kwon, S.-H.; Park, H.-S.; Kang, S.-W., Plasma-Enhanced Atomic Layer Deposition of Ruthenium Thin Films. *Electrochemical and Solid State Letters* **2004**, *7*, C46.

19. Jung, H. J.; Han, J. H.; Jung, E. A.; Park, B. K.; Hwang, J.-H.; Son, S. U.; Kim, C. G.; Chung, T.-M.; An, K.-S., Atomic Layer Deposition of Ruthenium and Ruthenium Oxide Thin Films from a Zero-Valent (1, 5-Hexadiene)(1-Isopropyl-4-Methylbenzene) Ruthenium Complex and O2. *Chemistry of Materials* **2014**, *26*, 7083-7090.

20. Salaün, A.; Newcomb, S. B.; Povey, I. M.; Salaün, M.; Keeney, L.; O'mahony, A.; Pemble, M. E., Nucleation and Chemical Transformation of Ruo2 Films Grown on (100) Si Substrates by Atomic Layer Deposition. *Chemical Vapor Deposition* **2011**, *17*, 114-122.

21. Cummins, C.; Ghoshal, T.; Holmes, J. D.; Morris, M. A., Strategies for Inorganic Incorporation Using Neat Block Copolymer Thin Films for Etch Mask Function and Nanotechnological Application. *Advanced Materials* **2016**, *28*, 5586-5618.

22. Frascaroli, J.; Cianci, E.; Spiga, S.; Seguini, G.; Perego, M., Ozone-Based Sequential Infiltration Synthesis of Al2o3 Nanostructures in Symmetric Block Copolymer. *ACS applied materials & interfaces* **2016**, *8*, 33933-33942.

23. Peng, Q.; Tseng, Y. C.; Darling, S. B.; Elam, J. W., Nanoscopic Patterned Materials with Tunable Dimensions Via Atomic Layer Deposition on Block Copolymers. *Advanced materials* **2010**, *22*, 5129-5133.

24. Peng, Q.; Tseng, Y.-C.; Darling, S. B.; Elam, J. W., A Route to Nanoscopic Materials Via Sequential Infiltration Synthesis on Block Copolymer Templates. *Acs Nano* **2011**, *5*, 4600-4606.

25. Ramanathan, M.; Tseng, Y.-C.; Ariga, K.; Darling, S. B., Emerging Trends in Metal-Containing Block Copolymers: Synthesis, Self-Assembly, and Nanomanufacturing Applications. *Journal of Materials Chemistry C* **2013**, *1*, 2080-2091.

26. Waldman, R. Z.; Mandia, D. J.; Yanguas-Gil, A.; Martinson, A. B.; Elam, J. W.; Darling, S. B., The Chemical Physics of Sequential Infiltration Synthesis—a Thermodynamic and Kinetic Perspective. *The Journal of chemical physics* **2019**, *151*, 190901.

27. Leng, C. Z.; Losego, M. D., Vapor Phase Infiltration (Vpi) for Transforming Polymers into Organic–Inorganic Hybrid Materials: A Critical Review of Current Progress and Future Challenges. *Materials Horizons* **2017**, *4*, 747-771.

28. Lee, S.-M.; Pippel, E.; Gösele, U.; Dresbach, C.; Qin, Y.; Chandran, C. V.; Bräuniger, T.; Hause, G.; Knez, M., Greatly Increased Toughness of Infiltrated Spider Silk. *Science* **2009**, *324*, 488-492.

29. Lee, S.-M.; Pippel, E.; Moutanabbir, O.; Gunkel, I.; Thurn-Albrecht, T.; Knez, M., Improved Mechanical Stability of Dried Collagen Membrane after Metal Infiltration. *ACS applied materials & interfaces* **2010**, *2*, 2436-2441.

30. Ocola, L.; Sampathkumar, V.; Kasthuri, N.; Winarski, R., Contrast Enhancement of Biological Nanoporous Materials with Zinc Oxide Infiltration for Electron and X-Ray Nanoscale Microscopy. *Scientific reports* **2017**, *7*, 1-8.

31. Segal-Peretz, T.; Winterstein, J.; Doxastakis, M.; Ramirez-Hernandez, A.; Biswas, M.; Ren, J.; Suh, H. S.; Darling, S. B.; Liddle, J. A.; Elam, J. W., Characterizing the Three-Dimensional Structure of Block Copolymers Via Sequential Infiltration Synthesis and Scanning Transmission Electron Tomography. *ACS nano* **2015**, *9*, 5333-5347.

32. Lee, S.; Subramanian, A.; Tiwale, N.; Kisslinger, K.; Mumtaz, M.; Shi, L.-Y.; Aissou, K.; Nam, C.-Y.; Ross, C. A., Resolving Triblock Terpolymer Morphologies by Vapor-Phase Infiltration. *Chemistry of Materials* **2020**, *32*, 5309-5316.

33. McGuinness, E. K.; Zhang, F.; Ma, Y.; Lively, R. P.; Losego, M. D., Vapor Phase Infiltration of Metal Oxides into Nanoporous Polymers for Organic Solvent Separation Membranes. *Chemistry of Materials* **2019**, *31*, 5509-5518.

34. Wang, W.; Chen, C.; Tollan, C.; Yang, F.; Qin, Y.; Knez, M., Efficient and Controllable Vapor to Solid Doping of the Polythiophene P3ht by Low Temperature Vapor Phase Infiltration. *Journal of Materials Chemistry C* **2017**, *5*, 2686-2694.

35. Wang, W.; Yang, F.; Chen, C.; Zhang, L.; Qin, Y.; Knez, M., Tuning the Conductivity of Polyaniline through Doping by Means of Single Precursor Vapor Phase Infiltration. *Advanced Materials Interfaces* **2017**, *4*, 1600806.

36. Knez, M.; Nielsch, K.; Niinistö, L., Synthesis and Surface Engineering of Complex Nanostructures by Atomic Layer Deposition. *Advanced Materials* **2007**, *19*, 3425-3438.

37. Barick, B. K.; Simon, A.; Weisbord, I.; Shomrat, N.; Segal-Peretz, T., Tin Oxide Nanostructure Fabrication Via Sequential Infiltration Synthesis in Block Copolymer Thin Films. *Journal of colloid and interface science* **2019**, *557*, 537-545.

38. Tseng, Y.-C.; Peng, Q.; Ocola, L. E.; Elam, J. W.; Darling, S. B., Enhanced Block Copolymer Lithography Using Sequential Infiltration Synthesis. *The Journal of Physical Chemistry C* **2011**, *115*, 17725-17729.

39. Zhou, C.; Segal-Peretz, T.; Oruc, M. E.; Suh, H. S.; Wu, G.; Nealey, P. F., Fabrication of Nanoporous Alumina Ultrafiltration Membrane with Tunable Pore Size Using Block Copolymer Templates. *Advanced Functional Materials* **2017**, *27*, 1701756.

40. Rahman, A.; Ashraf, A.; Xin, H.; Tong, X.; Sutter, P.; Eisaman, M. D.; Black, C. T., Sub-50-Nm Self-Assembled Nanotextures for Enhanced Broadband Antireflection in Silicon Solar Cells. *Nature communications* **2015**, *6*, 1-6.

41. Barry, E.; Mane, A. U.; Libera, J. A.; Elam, J. W.; Darling, S. B., Advanced Oil Sorbents Using Sequential Infiltration Synthesis. *Journal of Materials Chemistry A* **2017**, *5*, 2929-2935.

42. Azpitarte, I.; Knez, M., Vapor Phase Infiltration: From a Bioinspired Process to Technologic Application, a Prospective Review. *MRS Communications* **2018**, *8*, 727-741.

43. Ingram, W. F.; Jur, J. S., Properties and Applications of Vapor Infiltration into Polymeric Substrates. *Jom* **2019**, *71*, 238-245.

44. Ashurbekova, K.; Ashurbekova, K.; Botta, G.; Yurkevich, O.; Knez, M., Vapor Phase Processing: A Novel Approach for Fabricating Functional Hybrid Materials. *Nanotechnology* **2020**, *31,* 342001

45. Waldman, R. Z.; Jeon, N.; Mandia, D. J.; Heinonen, O.; Darling, S. B.; Martinson, A. B., Sequential Infiltration Synthesis of Electronic Materials: Group 13 Oxides Via Metal Alkyl Precursors. *Chemistry of Materials* **2019**, *31*, 5274-5285.

46. She, Y.; Lee, J.; Diroll, B. T.; Lee, B.; Aouadi, S.; Shevchenko, E. V.; Berman, D., Rapid Synthesis of Nanoporous Conformal Coatings Via Plasma-Enhanced Sequential Infiltration of a Polymer Template. *ACS omega* **2017**, *2*, 7812-7819.

47. Azpitarte, I.; Zuzuarregui, A.; Ablat, H.; Ruiz-Rubio, L.; López-Ortega, A.; Elliott, S. D.; Knez, M., Suppressing the Thermal and Ultraviolet Sensitivity of Kevlar by Infiltration and Hybridization with Zno. *Chemistry of Materials* **2017**, *29*, 10068-10074.

48. Peng, Q.; Tseng, Y.-C.; Long, Y.; Mane, A. U.; DiDona, S.; Darling, S. B.; Elam, J. W., Effect of Nanostructured Domains in Self-Assembled Block Copolymer Films on Sequential Infiltration Synthesis. *Langmuir* **2017**, *33*, 13214-13223.

49. Minjauw, M. M.; Dendooven, J.; Capon, B.; Schaekers, M.; Detavernier, C., Atomic Layer Deposition of Ruthenium at 100° C Using the Ruo 4-Precursor and H 2. *Journal of Materials Chemistry C* **2015**, *3*, 132-137.

50. Chou, T.; Prayoonthong, P.; Aitouchen, A.; Libera, M., Nanoscale Artifacts in Ruo4-Stained Poly (Styrene). *Polymer* **2002**, *43*, 2085-2088.

51. Trent, J. S.; Scheinbeim, J. I.; Couchman, P. R., Ruthenium Tetraoxide Staining of Polymers for Electron Microscopy. *Macromolecules* **1983**, *16*, 589-598.

52. Sun, Y.; Steinhart, M.; Zschech, D.; Adhikari, R.; Michler, G. H.; Gösele, U., Diameter-Dependence of the Morphology of Ps-B-Pmma Nanorods Confined within Ordered Porous Alumina Templates. *Macromolecular Rapid Communications* **2005**, *26*, 369-375.

53. Li, X.; Iocozzia, J.; Chen, Y.; Zhao, S.; Cui, X.; Wang, W.; Yu, H.; Lin, S.; Lin, Z., From Precision Synthesis of Block Copolymers to Properties and Applications of Nanoparticles. *Angewandte Chemie International Edition* **2018**, *57*, 2046-2070.

54. Minjauw, M. M.; Rijckaert, H.; Driessche, I. V.; Detavernier, C.; Dendooven, J., Nucleation Enhancement and Area-Selective Atomic Layer Deposition of Ruthenium Using Ruo4 and H2 Gas. *Chemistry of Materials* **2019**, *31*, 1491-1499.

55. Petit, R. R.; Li, J.; Van de Voorde, B.; Van Vlierberghe, S.; Smet, P. F.; Detavernier, C., Atomic Layer Deposition on Polymer Thin Films: On the Role of Precursor Infiltration and Reactivity. *ACS Applied Materials & Interfaces* **2021**, *13*, 46151-46163.

56. Cianci, E.; Nazzari, D.; Seguini, G.; Perego, M., Trimethylaluminum Diffusion in Pmma Thin Films During Sequential Infiltration Synthesis: In Situ Dynamic Spectroscopic Ellipsometric Investigation. *Advanced Materials Interfaces* **2018**, *5*, 1801016.

57. He, X.; Waldman, R. Z.; Mandia, D. J.; Jeon, N.; Zaluzec, N. J.; Borkiewicz, O. J.; Ruett, U.; Darling, S. B.; Martinson, A. B.; Tiede, D. M., Resolving the Atomic Structure of

Sequential Infiltration Synthesis Derived Inorganic Clusters. *ACS nano* **2020**, *14*, 14846-14860.

58. Metwalli, E.; Körstgens, V.; Schlage, K.; Meier, R.; Kaune, G.; Buffet, A.; Couet, S.; Roth, S. V.; Röhlsberger, R.; Müller-Buschbaum, P., Cobalt Nanoparticles Growth on a Block Copolymer Thin Film: A Time-Resolved Gisaxs Study. *Langmuir* **2013**, *29*, 6331-6340.

59. Ramalla, I.; Gupta, R. K.; Bansal, K., Effect on Superhydrophobic Surfaces on Electrical Porcelain Insulator, Improved Technique at Polluted Areas for Longer Life and Reliability. *Int. J. Eng. Technol* **2015**, *4*, 509.

60. Poonkottil, N.; Minjauw, M. M.; Werbrouck, A.; Checchia, S.; Solano, E.; Nisula, M.; Franquet, A.; Detavernier, C.; Dendooven, J., Atomic Layer Deposition of Ruthenium Dioxide Based on Redox Reactions between Alcohols and Ruthenium Tetroxide. *Chemistry of Materials* **2022**. doi.org/10.1021/acs.chemmater.2c02292.

61. Azoulay, R.; Shomrat, N.; Weisbord, I.; Atiya, G.; Segal-Peretz, T., Metal Oxide Heterostructure Array Via Spatially Controlled–Growth within Block Copolymer Templates. *Small* **2019**, *15*, 1904657.

62. Singh, A.; Knaepen, W.; Sayan, S.; El Otell, Z.; Chan, B. T.; Maes, J. W.; Gronheid, R. In *Impact of Sequential Infiltration Synthesis on Pattern Fidelity of Dsa Lines*, Advances in Patterning Materials and Processes XXXII, SPIE: 2015; pp 178-184.

63. Musschoot, J.; Xie, Q.; Deduytsche, D.; Van den Berghe, S.; Van Meirhaeghe, R.; Detavernier, C., Atomic Layer Deposition of Titanium Nitride from Tdmat Precursor. *Microelectronic Engineering* **2009**, *86*, 72-77.

64. Gatineau, J.; Yanagita, K.; Dussarrat, C., A New Ruo4 Solvent Solution for Pure Ruthenium Film Depositions. *Microelectronic Engineering* **2006**, *83*, 2248-2252.

65. Ahlrichs, R.; Bär, M.; Häser, M.; Horn, H.; Kölmel, C., Electronic Structure Calculations on Workstation Computers: The Program System Turbomole. *Chemical Physics Letters* **1989**, *162*, 165-169.

66. Perdew, J. P.; Burke, K.; Ernzerhof, M., Generalized Gradient Approximation Made Simple. *Physical review letters* **1996**, *77*, 3865.

67. Schäfer, A.; Horn, H.; Ahlrichs, R., Fully Optimized Contracted Gaussian Basis Sets for Atoms Li to Kr. *The Journal of Chemical Physics* **1992**, *97*, 2571-2577.

Table of contents